Planet. Space Sci., Vol. 35, No. 8, pp. 965–976, 1987
Printed in Great Britain.

0032-0633/87 $3.00 + 0.00
Pergamon Journals Ltd.

THE VELOCITY DISTRIBUTION FUNCTION OF THE NEUTRAL LITHIUM CLOUD PRODUCED BY AN *AMPTE* SOLAR WIND RELEASE

S. C. CHAPMAN
Queen Mary College, Mile End Road, London E1 4NS, U.K.

and

A. D. JOHNSTONE and A. J. COATES
Mullard Space Science Laboratory, University College London, Holmbury St Mary, Dorking, Surrey, U.K.

(*Received in final form* 2 *February* 1987)

Abstract—On 20 September 1984 a release of photoionizing lithium neutrals was made in the quiet solar wind, by the *AMPTE–IRM* spacecraft. The MSSL ion instrument on board the *UKS* spacecraft that was positioned ~ 30 km from the release centre enabled measurement of significant fluxes of lithium ions to be made for ~ 3 min after the release; that is, long after the initial (~ 25 s) local perturbation to the field and flow had died away. Here, we examine in detail the MSSL on detector response to the release ions, showing that the ion measurements are consistent with injection into a cycloidal orbit. Knowing the ion orbit it is then possible to trace the expansion of the neutral lithium cloud and obtain its initial velocity distribution. Various preliminary analyses suggested a shell-like expansion of the cloud, but disagreed over its velocity. The more detailed analysis of the *UKS* data presented here shows that it is not possible to determine from this data whether or not the cloud is shell-like, but reveals that significant local anisotropy is present.

1. INTRODUCTION

On 20 September 1984, a cloud of photoionizing lithium vapour was released in the solar wind in steady ambient conditions from the German *IRM* (*Ion Release Module*), upstream of the Earth's bow shock, as part of the *AMPTE* (*Active Magnetospheric Particle Tracer Explorers*) mission (e.g. Bryant *et al.*, 1985). Whilst the principal motive for this release was to trace the entry of particles into the magnetosphere a complementary investigation into the early time behaviour of the release plasma was possible using the instrumentation of the *IRM*, and that of the *UKS* (*United Kingdom Subsatellite*) located at ~ 30 km away (e.g. Lühr *et al.*, 1986; Coates *et al.*, 1986).

The expansion speed of the released neutrals was small, ~ 2.5 km s^{-1}, so that photoionization initially produced sufficient plasma densities to rapidly (within ~ $\frac{1}{2}$ s of the release time, 9:56:02 U.T.) supress the magnetic field to zero at the *IRM*. This diamagnetic cavity did not, however, extend to the *UKS* location, although the associated field and flow disturbance were subsequently seen at both spacecraft. At the *UKS*, the incoming lithium ions had arrival directions that were always easily distinguishable from the solar wind population. Accelerated lithium ions were first seen at the *UKS* close to the maximum enhancement of the magnetic field. Two 5 s spacecraft spins later, however (at 9:26:25 U.T.), the ambient field and flow had almost returned to their steady, pre-release values. Since the timescale of this initial disturbance (~ 25 s) was much shorter than the photoionization timescale of lithium, ~ 1 h, most of the released neutrals were ionized at low local mass densities, behaving as test ions in the undisturbed ambient field and flow. These ions were seen at the *UKS* for ~ 2.75 min after the initial disturbance had died away, always arriving within one 45° azimuthal and 67.5° polar bin of the ion detector. In the prevailing steady ambient field and flow the test ion motion of the photoionized lithium is simple to determine [the only other release of this kind (on 11 September) took place in the presence of large amplitude upstream waves so that an analysis similar to that given here cannot be performed]. Measurements of the differential energy flux of these lithium ions obtained by the MSSL ion instrument on board the *UKS* (Coates *et al.*, 1985) can then be used to infer the time-dependent neutral lithium number densities in the regions where the observed ions were created. This then allows the velocity distribution function of the collisionless neutral cloud to be determined over a restricted region in velocity space.

In this paper we will therefore begin in the next section by deriving a simplified relationship between

the lithium ion fluxes measured at the *UKS*, and the velocity distribution function of the expanding neutral cloud required to produce them. We then address the relevant details of the *UKS* instrumentation in Section 3, with a view to assessing the uncertainties and restrictions on the measured quantities required for our derivation of the neutral $f(\mathbf{v})$. Finally, the features of the neutral velocity distribution function found for the lithium release will be discussed in Section 4.

2. IDEAL DERIVATION OF THE NEUTRAL VELOCITY DISTRIBUTION

Each release is made using two canisters, the mixture of lithium metal and copper oxide that they contain being ignited when the canisters are ~ 2 km apart (Haerendel *et al.*, 1985), a distance that can be neglected in comparison with the *UKS–IRM* separation so that the neutral cloud behaves as if created at a single point in space. All of the lithium vapour ($\sim 3 \times 10^{25}$ atoms) leaves the canisters within $\sim \frac{1}{5}$ s with the canisters igniting within a fraction of a second of each other also (G. Haerendel, private communication). The neutrals hence behave as if they were all produced simultaneously, since the above time intervals are short in comparison with, for instance, the time taken for the neutral cloud to expand to a radius where significant ion fluxes are detected at the *UKS* (~ 15 s). We can now estimate the time after the release when the cloud becomes collision free. Assuming that the neutrals fill a spherical volume, with radius increasing with the typical expansion speed of a few kilometres per second and taking the collision cross-section $\sigma \sim 10^{-15}$ cm^2 gives times < 0.3 s which is of order the time taken for all of the neutrals to be ejected from the canisters. The neutrals hence expand freely away from the release point with an unchanging velocity distribution, which will always specify their number density distribution at any later time.

The expansion speed of the neutrals, $\sim$ a few kilometers per second, is small, compared with the typical speeds of the lithium ions seen at the *UKS* ($\sim$ 50–200 km s^{-1}). Given that the solar wind **E** and **B** vectors are constant over the ion time of flight, the motion of the newly created ions is almost exactly cycloidal. It is convenient to introduce orthogonal coordinates α in the electric field direction (where $\mathbf{E} = -\mathbf{v}_{sw} \wedge \mathbf{B}$) and β in the $\mathbf{E} \wedge \mathbf{B}$ direction, the ion motion then being confined to the α, β plane. The ion equations of motion are then:

$$v_\alpha = v_\perp \sin \Omega t \tag{1}$$

$$v_\beta = v_\perp (1 - \cos \Omega t) \tag{2}$$

which integrate to give:

$$r_\alpha = \frac{v_\perp}{\Omega}(1 - \cos \Omega t) + r_{\alpha 0} \tag{3}$$

$$r_\beta = \frac{v_\perp}{\Omega}(\Omega t - \sin \Omega t) + r_{\beta 0} \tag{4}$$

where $(r_{\alpha 0}, r_{\beta 0})$ is the point where the ion was created, $v_\perp$ is the speed of gyration about the field $|\mathbf{E} \wedge \mathbf{B}|/B^2$ and Ω is the gyrofrequency eB/m. From equations (1) and (2) it is clear that the maximum ion velocity $2\,v_\perp$ is achieved half a gyroperiod after the ion is created. Now for the second lithium release $2v_\perp \approx 2v_{sw} \simeq 900$ km s^{-1}, which is much larger than the typical speeds with which the ions arrive at the *UKS*, implying that they are seen during the early part of their cycloidal motion. For small Ωt equations (1)–(4) become

$$v_\alpha \approx v_\perp \Omega t \tag{5}$$

$$v_\beta \approx 0 \tag{6}$$

$$r_\alpha \approx r_{\alpha 0} + v_\perp \Omega \frac{t^2}{2} \tag{7}$$

$$r_\beta \approx r_{\beta 0} \tag{8}$$

which then just describe the motion of an ion accelerating from rest in an electric field $\mathbf{E} = -\mathbf{v}_{sw} \wedge \mathbf{B} = -v_\perp B \hat{\boldsymbol{\alpha}}$ which is constant over its time of flight. If the ambient conditions are sufficiently steady, as we shall see is the case for the second lithium release, we can further assume that the direction of the electric field vector, and hence the Li ion motion, is constant over the entire interval during which test ions were detected at the *UKS*. The geometry of this idealized calculation is given in Fig. 1, which shows the plane containing the *UKS*, the *IRM* (i.e. the spacecraft separation vector **s**) and the static electric field direction vector $\hat{\mathbf{E}}$. After release, lithium neutrals move radially from the *IRM*. Those which are subsequently detected after ionization will have moved along paths such as **r**, being ionized at C as they cross $\hat{\mathbf{E}}$ to be accelerated along a straight line orbit to the *UKS* position. The path length of these ions P (from point C to the *UKS*) is just given by the energy ε with which they are detected (ε will be in electron volts throughout), and by the slowly varying electric field magnitude so that $P = \varepsilon/|\mathbf{E}(t)|$. Hence **s** and a particular P of any ion arriving at the *UKS* completely specify the path **r** of its earlier motion as a neutral. The set of discrete energy bins ε_i, with widths $\mathrm{d}\varepsilon_i$ of the ion detector, can be used to define a set of fixed path length bins along $\hat{\mathbf{E}}$, with centres at $P_i = \varepsilon_i/\bar{E}$, and widths $\mathrm{d}P_i = \mathrm{d}\varepsilon_i/\bar{E}$, where $\bar{E}$ is the mean electric

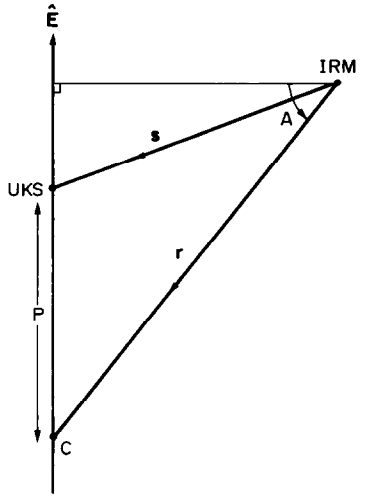

FIG. 1. THE GEOMETRY OF BOTH THE LITHIUM NEUTRAL AND ION PATHS IS SHOWN W.R.T. THE SPACECRAFT POSITIONS, IN THE **E**, **s** PLANE.
The neutrals are released approximately at the *IRM* position, and travel along paths such as **r**. Ions seen at the *UKS* at a given energy were then produced from neutrals that were photoionized as they crossed the electric field vector **E** passing through the *UKS*. The ion creation point relative to the spacecraft position is specified by the location of the separation vector **s**, and the ion path length P along **E**.

field magnitude. The time-dependent energy $\varepsilon_i(t)$ of ions which are all regarded to have travelled the same fixed path length P_i will then just be such that their path length $P = \varepsilon_i(t)/|\mathbf{E}(t)|$ lies within a distance $dP_i/2$ of P_i. Now, the neutral number density as a function of time at a particular fixed point specified by P_i and **s** will just depend on the velocity distribution of neutrals that move along the appropriate direction **r**. By measuring the fluxes of ions within given energy bins $\varepsilon_i(t)$ appropriate to a particular P_i we therefore deduce the velocity distribution function of neutrals moving in a given direction. The entire range of fixed points P_i, defined by the energy range of the instrument, then gives the range of directions (or angles A on Fig. 1) over which the neutral velocity distribution function can be determined, all of which lie in the **Ê**, **s** plane.

Using the geometry of Fig. 1 we can now explicitly derive the relationship between the ion energy fluxes detected at the *UKS* as a function of time, and the neutral velocity distribution function. At the time of the release ($t = 0$) the collisionless neutral population is produced with velocity distribution $f(\mathbf{v})$, which is normalized such that the total number of neutrals at velocity **v** and in velocity space volume d^3v is just $N_0 f(\mathbf{v})\,d^3v$, where N_0 is the total remaining number of neutrals. The local neutral number density $n(\mathbf{r}, t)$ may be related to the velocity distribution function $f(\mathbf{v})$ as follows. First, at the time of the release the number of neutrals with speeds v–$v+dv$ within solid angle $d\Omega$, is just

$$dn = N_0 f(\mathbf{v}) v^2\,dv\,d\Omega \tag{9}$$

where N_0 is the total number of released neutrals, and is to a good approximation constant over the ~ 3 min during which ions are detected at the *UKS*, since this is much shorter than the photoionization time $\tau_p \simeq 1$ h. At time t after the release, the same number of neutrals dn will have expanded radially to reach distance r–$r+dr$ such that $r = vt$, occupying a volume

$$V = r^2\,dr\,d\Omega = t^3 v^2\,dv\,d\Omega. \tag{10}$$

The neutral number density is hence

$$n(\mathbf{r}, t) = \frac{dn}{V} = N_0 \frac{f(\mathbf{r}/t)}{t^3}. \tag{11}$$

Now the flux of ions arriving at the detector $F_i(\varepsilon, t)$ $m^{-2}\,s^{-1}\,eV^{-1}$ per unit energy range is just the number of ions created over a length $|E(t)|^{-1}$ parallel to the electric field at a constant rate τ_p^{-1}, a flight time $t_A(\varepsilon)$ earlier:

$$F_i(\varepsilon, t) = \frac{n(\mathbf{r}, t - t_A)}{|\mathbf{E}(t)|\tau_p}.$$

Hence

$$f(\mathbf{v}) = \frac{(t - t_A)^3 |\mathbf{E}(t)|\tau_p}{N_0} F_i(\varepsilon, t). \tag{12}$$

The flux is measured by the positive ion detector as a number of particles counted N_c in the sample time τ_s, so that $F_i(\varepsilon, t) = N_c/\varepsilon\tau_s G(\theta_0, \phi_0)$. The term $G(\theta_0, \phi_0)$ is the response of the detector to a beam in the direction (θ_0, ϕ_0) and has the dimensions of area (m^2). Hence

$$f(\mathbf{v}) = \frac{(t - t_A)^3 |\mathbf{E}(t)|\tau_p}{N_0} \frac{N_c}{\varepsilon\tau_s G(\theta_0, \phi_0)} (m^{-3}\,s^3) \tag{13}$$

where

$$G(\theta_0, \phi_0) = 2.37 \times 10^{-8}\,m^2$$

$$\tau_s = 4.9 \times 10^{-3}\,s.$$

It will be shown that the most significant departures from the assumptions implicit in equation (13) are the uncertainty in the orientation of the spacecraft separation vector **s**, the deviation of the cycloidal ion trajections from straight line orbits, and the non contiguous coverage of the ion detector. We will address these (and other less important factors which are taken into account in the analysis) in the following sections. The remaining possible sources of error, which we have found to be negligible, are briefly listed in Appendix A.

3. INSTRUMENTATION AND SOURCES OF UNCERTAINTY

We will first briefly introduce the magnetometer experiment on board the *UKS*, and the method of the determination of **s**, before proceeding with the more detailed discussion of the ion detector itself. The Imperial College fluxgate magnetometer (Southwood *et al.*, 1985) measures the ambient magnetic field vector components along a set of three non coplanar axes, and at a rate of 16 samples s^{-1}. The uncertainty in the magnetic field measurements are $\sim \pm 0.1$ nT on the off spin axis components and $\sim \pm 0.2$ nT along the spin axis (W.A.C. Mier-Jedrzejowicz, private communication, 1985). At the time of the release, radar ranging between the *UKS* and *IRM* was used to determine the spacecraft scalar separation, although the orientation of **s** could only be inferred from ground-based orbit determination. The scalar separation is then 32 ± 2.5 km, with less accurately determined GSE components (17.5, −3.9, −14.0) km with errors of $\sim \pm 30\%$ in x and z, and $\sim \pm 200\%$ in y (G. Spalding, private communication, 1985). Now from Fig. 1, since the neutral velocity is

$$\mathbf{v} = \frac{r}{t} = \frac{(\mathbf{s} - P\hat{\mathbf{E}})}{t} \tag{14}$$

the error in **s** will contribute most significantly where Li ion data is used to determine the neutral $f(\mathbf{v})$ for which the ion path length $P < |\mathbf{s}|$. In comparison, lithium test ions seen after the second release typically have energies $\sim$ 500 eV–1.5 keV, corresponding to $P \sim$ 120–400 km. We will assess in detail the effect of the uncertainty in **s** on the entire neutral $f(\mathbf{v})$ in Section 4.

3.1. *Ion detector response*

The Mullard Space Science Laboratory positive ion experiment on *AMPTE–UKS* (Coates *et al.*, 1985) consists of two electrostatic analysers, each with a field of view $112.5° \times 5°$, mounted back-to-back, viewing tangentially to the spacecraft and, between them, covering the complete angular range from 0° to 180° with respect to the spin axis. As the spacecraft makes one revolution in 5 s, the full 4π solid angle is covered. The energy of the analyser is swept through the range from 20 keV/q to 10 eV/q precisely 16 times each revolution. The instrument can be operated in a number of data accumulation programmes. During the lithium release of 20 September 1984 it was in the SW2 programme (Coates *et al.*, 1985) in which it is switched to a particular high resolution mode for the 45° sector centred on the solar direction on alternate spins. The energy is then swept over one quarter of the usual energy range four times as often, i.e. eight times, in that sector. At the same time the polar angular resolution and the energy resolution are improved. In the normal mode, used in the remainder of the programme, the polar angle range is divided into four zones, and the azimuthal measurements are collected into eight sectors. In essence, the instrument covers its full energy and angular range once every 5 s and in addition, once every 10 s it makes an accurate observation of the solar wind bulk velocity (with an uncertainty of $\sim \pm 4$ km s^{-1} in magnitude, and $\sim$ 1–2° in direction). In the normal mode the energy sweep repeats every 22.5° in the spacecraft rotation, but the angle of acceptance in the azimuthal direction is only 5° full width at half maximum. Consequently, azimuthal coverage at a given ion energy will, in general, be incomplete. We will now examine the effectiveness with which the lithium test ions moving in their cycloidal orbits are detected, by comparing the azimuthal angles at which they arrive at the *UKS* with ion instrument efficiency as a function of azimuthal angle.

The expression for the azimuthal angle of the look direction of the detector centre, ϕ_d, in terms of the ion energy ε that it measures is simple to obtain. The detector is spin synchronized, so that incoming ions of a given energy are always sampled when the detector centre is at 16 particular azimuthal angles during each spin, which do not precess by more than $\sim \frac{1}{2}°$. Now ϕ_d is measured in the spacecraft coordinate system in which the spacecraft spin axis points along the z axis, with the spacecraft x axis lying in the plane parallel to the x, z GSE plane. Each spin starts ($\phi_d = 0$) when the detector centre points along this spacecraft x axis, ϕ_d increasing in the anticlockwise sense as the spacecraft spins. In each 1/16th of a spin the detector sweeps from 20 keV to 10 eV logarithmically, in 60 equal time intervals (with four further time intervals at the beginning of each sweep during which no measurement is made). The separation in spacecraft azimuth between subsequent energy measurements is just $22.5/64 = 0.352°$. If B denotes the number of the energy sweep (the first sweep at $B = 0$), we then have

$$\phi_d(\varepsilon) = 22.5B + \left(\frac{\log_{10}\varepsilon - 1}{m} + 63\right)\Delta\phi \text{ degrees} \tag{15}$$

where

$$m = -\left(\frac{3 + \log_{10} 2}{59}\right).$$

The variation of the detector efficiency over its $\sim 5°$ acceptance angle is approximately Gaussian; here it is sufficient to simply consider the angle at which it reaches FWHM, and at which it falls below 10% of the maximum. These angles vary sufficiently slowly

over the polar angle of the detector that we use one set of values appropriate for the mean polar angle of the incoming lithium ions if moving on cycloidal orbits. Finally, we will transform the angles calculated above from the spacecraft to the GSE coordinate system in order to allow a comparison with the expected azimuthal arrival angles of the Li ions if moving on cycloidal orbits, expressions for which are given in Appendix B (at this time the spacecraft spin axis was at GSE angles $\theta = 7.8°$, $\phi = 280°$, to within $\frac{1}{2}°$). This will yield the range of energies of those incoming ions which would be expected to be seen by the detector, as a function of time. This comparison is illustrated by Fig. 2, which covers the range of energies over which almost all of the ions are detected. The range of GSE azimuth covered by the plot corresponds to the angle through which the detector turns during three of the 16 sweeps through its energy range made per spin. The GSE azimuthal angles of the detector FWHM and "edges" (i.e. where its efficiency falls to 10% of maximum) are shown by the three pairs of short and long dashed lines, respectively. The shaded regions enclosed by these lines hence mark the "windows" or acceptance ranges in ε and ϕ of the detector. The set of solid lines then indicates the time-dependent energies and arrival angles of ions moving on cycloidal orbits, as given by equations (B3) and (B7). These lines have been drawn for solar wind velocity values and 5-s averages of the field obtained on those alternate spins when the solar wind velocity is accurately measured. Finally, the energies at which lithium ions (> 1 count) were observed in each of these alternate spins are marked with triangles along these lines. The single 45° azimuthal sector in which Li ions were seen (after 9:56:25 U.T.) corresponds to the lower two of the detector "windows" shown on the plot. The azimuthal arrival angles of these ions predicted by cycloidal motion in the slowly varying ambient fields can be seen to fall within an appropriate detector "window", to $\sim 1°$. This discrepancy is found to correspond to the effect of uncertainties in the measured field and flow vectors, and the spacecraft spin axis orientation.

Our analysis of the ion detector response so far has shown for the first time that the field and particle measurements made by the *UKS* during the quiet conditions following the second release are consistent with lithium ions produced from the expanding neutral cloud moving on cycloidal orbits, to a good approximation. It is also important to note from Fig. 2, however, that not all ions moving on cycloidal trajectories will be detected at the *UKS*. Since the energies of incoming ions at a given time specify the points in space where they were created [from equations (1) and (2)] and hence the velocities **v** of their source neutrals (e.g. see Fig. 1), the detector windows shown in Fig. 2 correspond to strips in velocity space where the neutral distribution function may be determined from the ion measurements. The effect of this constraint on the determination of the neutral velocity distribution function will be discussed in Section 4.

3.2. *Deviation due to exact cycloidal motion*

We will now finally calculate the error that the straight line orbit approximation used in Section 2 introduces into the derived neutral velocity vector **v**. In Fig. 3 the cycloidal path of an ion is drawn with respect to the $\hat{\boldsymbol{\alpha}}$, $\hat{\boldsymbol{\beta}}$ ($\hat{\mathbf{E}}$, $\mathbf{E} \wedge \mathbf{B}$) axes. The ion is created at the origin 0 [i.e. at $(r_{\alpha 0}, r_{\beta 0})$] and is detected with velocity **v** at the *UKS* as its trajectory passes through the point D [at (r_α, r_β)]. If the ion was assumed to have travelled along the electric field in a straight line, as given by equations (5)–(8), its approximate creation point would lie at Q. The separation between Q and the exact creation point (which is exaggerated in Fig. 3) is then specified by the angle $\gamma = \mathrm{ODQ}$ and the distance ratio $R = (\mathrm{OD} - \mathrm{DQ})/\mathrm{OD}$. Now

$$\tan\gamma = \frac{r_\beta - r_{\beta 0}}{r_\alpha - r_{\alpha 0}} = \frac{\Omega t - \sin\Omega t}{1 - \cos\Omega t} \tag{16}$$

from equations (3) and (4), and

$$R \simeq 1 - \cos\gamma. \tag{17}$$

Equation (B2) then relates γ and R directly to the ion energy as it reaches point D. Ion energies $\varepsilon \sim 1.5$ keV then give $\gamma \simeq 10°$ and $R \simeq 1.5\%$, which of course decrease with ε. This error in the location of the ion creation point translates directly to an error in the path **r** of its source neutral (see Fig. 1). We can, however, clearly neglect the error R for the typical range of ion energies of 1.5 keV or less, in comparison with the other uncertainties. This will not be the case for the angular displacement γ, which for ions created at large distances from the *UKS*, with corresponding vectors **r** at large angles A (see Fig. 1), translates directly to a significant displacement in A. We discuss the effect of this on the derived $f(\mathbf{v})$ in the next section.

4. RESULTS

The neutral velocity distribution function $f(\mathbf{v})$ has been calculated for neutrals travelling along a set of fixed radial paths **r** (such as in Fig. 1) which (for a given $\hat{\mathbf{E}}$ and **s**) are defined by the set of fixed path lengths $P_i = \varepsilon_i/\bar{E}$, where ε_i are the set of energy bins of the detector, and $\bar{E}$ is the mean electric field magnitude $\bar{E} = 3.92$ mV m^{-1}. This set of neutral paths **r** is just equivalent to a set of radial cuts in the **E**, **s** plane in

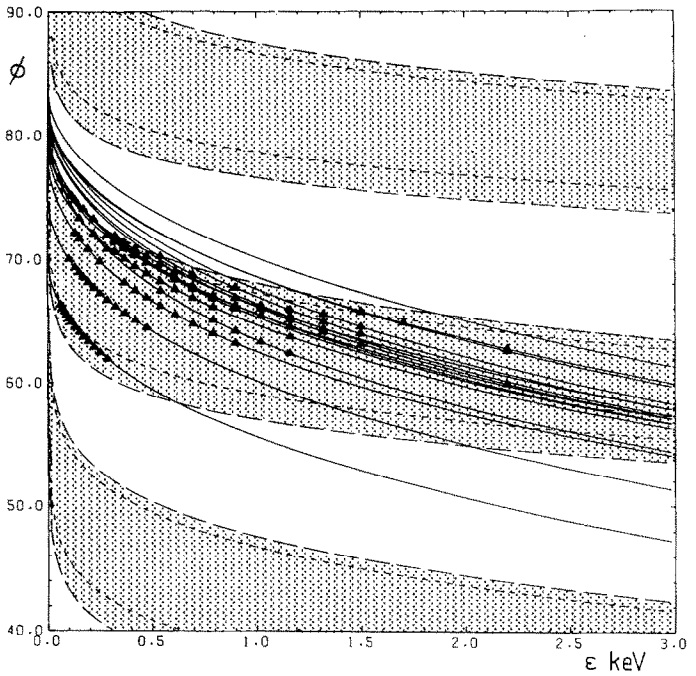

FIG. 2. THE FIGURE PROVIDES A COMPARISON BETWEEN THE GSE AZIMUTHAL COVERAGE OF THE ION INSTRUMENT, AND THE INCOMING GSE AZIMUTHAL DIRECTIONS OF LITHIUM IONS MOVING ON CYCLOIDAL ORBITS, AS A FUNCTION OF ENERGY (IN KILOELECTRONVOLTS).
The GSE azimuthal angles of the FWHM of the detector efficiency are marked by the three pairs of short dashed lines, and alongside these the long dashed lines mark the effective edges of the detector field of view, all of which are appropriate to the polar angles of incoming ions moving on cycloidal orbits. Each of the three shaded strips, or "windows" shown therefore represents one of the 16 sweeps in energy made by the detector during each spin. The solid lines then denote the azimuthal angles at which lithium ions arrive with a given energy, if moving on cycloidal orbits in the ambient electromagnetic fields seen at the *UKS* during the time period following the second release. Finally, the energies at which two or more lithium counts were actually observed during these spacecraft spins are marked on the curves by triangles.

velocity space $\mathbf{v} = \mathbf{r}/t$. We will begin by examining the properties of the neutral $f(\mathbf{v})$ along some examples of these cuts in velocity space, before combining the entire set to give a contour plot of $f(v)$. Figure 4 shows two examples of these cuts in velocity space, corresponding to energy bin numbers 26 (upper plot) and 34 (lower plot) of the ion detector, where bin number 1 is 20 keV, and number 60 is 10 eV. Now for each fixed cut in velocity space, and fixed $\mathbf{r}$ the speeds of the neutrals $|\mathbf{v}| = |\mathbf{r}|/t$, so that during each spacecraft spin a measurement of the neutral distribution function $f(\mathbf{v})$ along the cut is made at a particular speed $|\mathbf{v}|$. As well as marking the neutral speeds (in kilometers per second) along the bottom of the plots, we have also for reference marked at the top of the plot some of the appropriate spacecraft spin numbers. The first measurement that is used in this study, "spin 1" (beginning at 9:56:25 U.T.), then effectively sets an upper limit to the range of velocities over which $f(\mathbf{v})$ may be determined (given more exactly here, however, by the upper bound of the range of speeds $dv = dr/t$ covered by the first measurement). For the upper plot this upper limit is then ~ 9.5 km s^{-1} and for the lower plot is ~ 3.9 km s^{-1}. Having chosen a fixed set of cuts (with fixed $P_i = \varepsilon_i/\bar{E}$), each value of $f(\mathbf{v})$ at each spin within a given cut is calculated from the ion data within the appropriate energy bin $\varepsilon_i(t)$ which will vary from spin to spin with the electric field magnitude. In this way all the factors in equation (13) which vary with detected ion energy are also treated as time-dependent quantities. The normalized neutral velocity distribution function $f^*(\mathbf{v})$ has been plotted vs $\mathbf{v}$ in the figure, where

$$f(\mathbf{v}) = f^*(\mathbf{v}) \frac{\tau_p}{N_0 G_0} \text{m}^{-3}\text{s}^3 \tag{18}$$

where

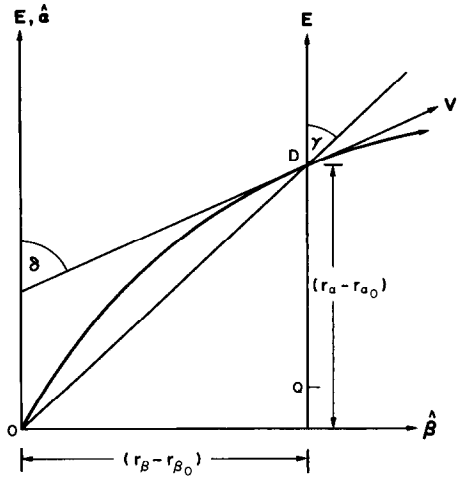

FIG. 3. THE RELATIONSHIP BETWEEN THE EXACT AND APPROXIMATE CREATION POINTS OF A TEST ION.
The exact cycloidal motion of the ion, shown here in the $\hat{\alpha}$, $\hat{\beta}$ plane (in which it is confined) begins at point O. If the ion is detected at point D along its trajectory, its approximate point of creation will lie a distance DQ along the $-\mathbf{E}$ direction, since the approximate ion motion is simply acceleration in the ambient electric field E.

$$f^*(\mathbf{v}) = (t-t_A)^3 \frac{E(t)}{\varepsilon} N_c S$$

and

$$G_0 = SG(\theta_0, \phi_0)\tau_s$$

the scaling factor $S = 1.355 \times 10^2$ appearing as a normalization constant for the plots, and including a later refinement of the calibration values.

A lower limit to the range in v space over which we can determine $f(\mathbf{v})$ is given by the ion instrument "one count level" [$N_c = 1$ in equation (13)] marked by the dashed lines on the plot; effectively $f^*(\mathbf{v})$ cannot be determined in the region below this line. The uncertainty with which the normalized values of $f(\mathbf{v})$ are known is principally just the statistical fluctuation in the number of counts involved in each measurement. We therefore average over adjacent measurements of $f^*(\mathbf{v})$, made during successive spacecraft spins, resulting in a loss of resolution in velocity space. The loss of resolution in v is minimized by averaging over a sufficient number of spins such that each resulting averaged measurement of $f^*(\mathbf{v})$ is always comprised of at least six counts, giving a maximum uncertainty in $f^*(\mathbf{v})$ of $\sim 40\%$. The actual number of counts corresponding to each of the measurements of $f^*(\mathbf{v})$ shown in Fig. 4 has been marked on the curves as an indication of their statistical significance. Strictly speaking, the averaging process described above

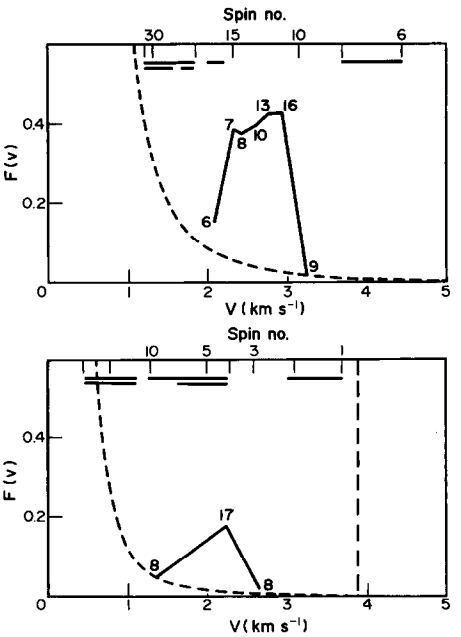

FIG. 4. TWO EXAMPLES OF RADIAL CUTS THROUGH THE NORMALIZED NEUTRAL VELOCITY DISTRIBUTION $f^*(\mathbf{v})$ IN THE E, s PLANE.
The normalization of $f^*(\mathbf{v})$ is given in the text, and velocities are in kilometers per second with their equivalent spacecraft spin numbers given across the top of each plot. The angles A of these cuts are 84.7° for the upper plot and 76.7° for the lower plot. The solid line denotes the neutral $f^*(\mathbf{v})$ itself, where the number of counts from which each averaged sample of $f^*(\mathbf{v})$ is comprised is given beside each point. The upper limit to the region within which $f(\mathbf{v})$ may be determined (see text) is marked by the vertical dashed line on the lower plot (and is outside the range of velocities of the upper plot); the lower limit which is approximately given by the one-count level is marked by the dashed curves. Finally, those spacecraft spins during which ions of the particular energies used to create these plots are not expected to fall within the detector "field of view" are marked with double horizontal bars across the top of the plot, and those spins during which ions are expected to arrive outside the detector FWHM are marked with single horizontal bars.

defines a new one-count level but from simple considerations this can be seen to be approximately the same as that obtained for the unaveraged case.

One final limitation on the region in velocity space in which $f(\mathbf{v})$ may be determined, is imposed by the incomplete angular coverage of the ion detector discussed in Section 3.1. At certain times ions arriving at the *UKS* with particular energies, that travelled on cycloidal orbits given by the observed ambient fields, will be at azimuthal angles which lie outside the ion detector field of view. We would therefore not expect to detect ions at these particular energies and times at the *UKS*, and this has indeed been shown to be the

case to within the uncertainties with which the various parameters are known. Furthermore, we would expect to measure reduced fluxes of ions that arrive at azimuthal angles where the detector efficiency is still substantial, but has fallen for instance below FWHM as shown on Fig. 2. We can now illustrate the effect of this reduction in the incoming ion fluxes on the measurement of the neutral $f(\mathbf{v})$. For each spacecraft spin during the entire period within which test ions were observed (that is, up to spin 33), the energy ranges over which the azimuthal arrival angles of ions on cycloidal orbits lie outside the detector "field of view" and FWHM are first determined. The spins during which the time-varying energies $\varepsilon = P_i|\mathbf{E}(t)|$, appropriate to each cut in velocity space, lie within the above energy ranges can then be found, and have been marked on the examples shown in Fig. 4 with the thick bars underneath the corresponding spin numbers, double bars referring to ions arriving outside the "field of view", and single bars to those arriving outside the FWHM. The magnitude of the neutral velocity distribution function would then be expected to be reduced over the ranges of velocities corresponding to these times. Looking first at the upper plot, we see that the cut through the distribution function shown is negligibly small for $v > 3.2$ km s^{-1}, rising at lower speeds to peak at $v \sim 2.8$–3.0 km s^{-1}. At ~ 2.2 km s^{-1} the magnitude of the distribution function can be seen to decrease from the peak value, but since this coincides with a region in velocity space which corresponds first to reduced, and then to negligible measured ion fluxes as the spin number increases, it is not clear that $f^*(v)$ actually falls away at these lower speeds. The speed at which $f^*(v)$ peaks must hence be regarded as a typical rather than the most probable speed. Our second example, shown in the lower plot, is a cut in v space which is at a smaller angle A (see Fig. 1). Here once again $f^*(v)$ is generally small at those speeds that correspond to measurements of negligible ion fluxes. Uncertainties in the location of the double bars on the plot (due principally to extrapolating between solar wind measurements that are only made accurately on alternate spins), do not allow us to attach any significance to the fact that the largest measurement of $f(\mathbf{v})$ occurs at the "edge" of the double bar region. It is interesting to note, however, that $f^*(v)$ also falls to a negligibly small value within the region 2.25 km s$^{-1} < v < 3.05$ km s^{-1}, where the detector efficiency is not reduced. By comparison, in the cut shown in the upper panel $f^*(v)$ appears to peak within this region, indicating that the neutral distribution is anisotropic.

Figure 4 shows cuts through the distribution function that are obtained for the most probable orientation of the spacecraft separation vector **s** (see Section 3). We can now combine all 60 of the cuts in the **E**, **s** plane in velocity space, calculated assuming the same orientation of **s**, to produce a contour plot of the neutral velocity distribution function. The effect on the features of the plot of the uncertainty in **s**, and of the deviation of cycloidal orbits from the approximation of straight line ion motion, will then be established. The contours of the normalized neutral velocity distribution function $f^*(\mathbf{v})$ in the **E**, **s** plane are shown in the left-hand plot of Fig. 5, drawn in steps of 0.1. Some of the positions of the cuts in the **E**, **s** plane along which $f(\mathbf{v})$ has been determined are also shown, labelled with the number of their defining energy level $\varepsilon_i = P_i\bar{E}$, the region over which $f(\mathbf{v})$ can be found extending in angle from cut 1 to cut 60. The upper boundary to the radial extent of this region, given by the measurement made at spin 1, is marked by the solid line on the left-hand side of the diagram. At lower velocities, the contours end as the magnitude of $f^*(\mathbf{v})$ falls below the one-count level. The regions corresponding to azimuthal arrival angles of ions lying outside the detector "field of view", and FWHM, have also been determined for all 60 cuts in velocity space, and are shown by the solid and hatched regions respectively in the centre plot on Fig. 5, also in the same format as the left-hand plot. The extent of these regions has been mapped from the spin 1 line to the edge of the shaded region nearest the **E** axis, extending to within the region where the one-count level is large.

Finally, these shaded regions are shown superimposed on the contours of $f^*(\mathbf{v})$ in the right-hand plot. It can then be seen that regions where the measured ion fluxes are reduced or expected to be zero correspond closely to regions where the magnitude of $f^*(\mathbf{v})$ is small, implying that the detector response is indeed modifying the distribution function that is observed. We therefore cannot expect to measure the value of $f(\mathbf{v})$ within the regions that are modified in this way so that, for instance, it cannot be discerned from the ion data whether the distribution function is shell-like, or whether it continues to have large values closer to the origin. Two features of the distribution function are, however, apparent from Fig. 5. First, as suggested from Fig. 4, it is clear that the distribution function is not isotropic, with typical speeds varying with direction from ~ 2.8 to ~ 2.1 km s^{-1} over the region spanning $\sim 17°$ in angle A where $f(\mathbf{v})$ may effectively be determined. Second, in the regions where $f(\mathbf{v})$ is measured at higher speeds, it has values which can be seen to be approximately a factor of two larger than those measured at lower speeds.

The average magnitude of the distribution function

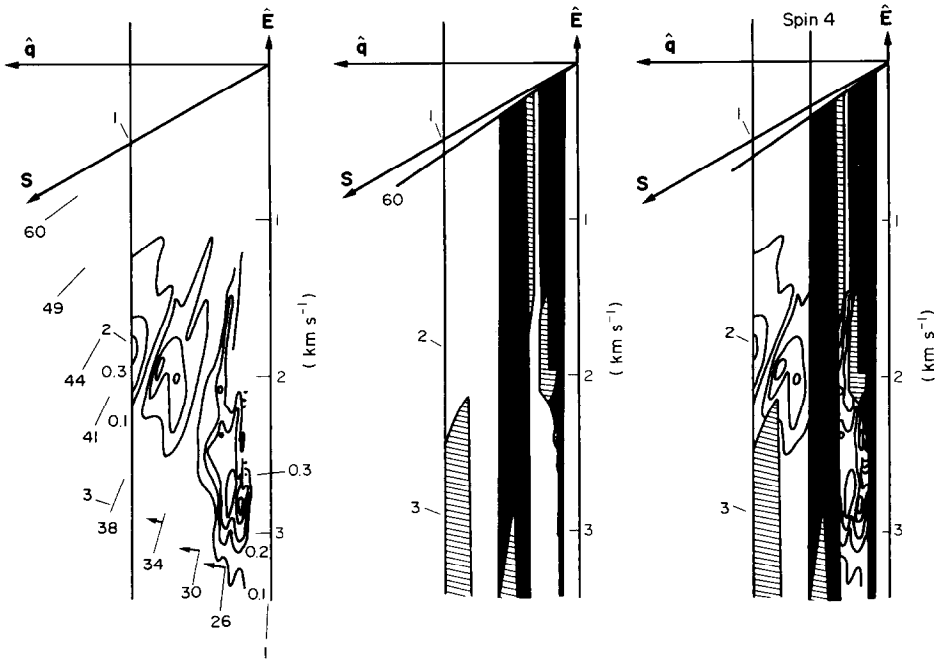

FIG. 5. LEFT-HAND PANEL: THE ENTIRE SET OF CUTS IN VELOCITY SPACE HAS BEEN COMBINED TO PRODUCE A CONTOUR PLOT OF THE NEUTRAL $f^*(\mathbf{v})$ OVER A LIMITED REGION IN THE **E**, **s** PLANE.

The **E** and **s** directions are shown on the plot, along with the angular directions of some of the cuts, each of which is marked with the number of its defining energy level (see text). The contours of $f^*(\mathbf{v})$ are in steps of 0.1 and have been drawn up to the one-count level. The neutral $f^*(\mathbf{v})$ can be sampled over a region in this plane extending radially up to the speeds defined by the first measurement in time used in this study (solid line) and extending in angle from the cut defined by the highest energy level of the instrument (No. 1 equivalent to 20 keV) to the lower level (No. 60 equivalent to 10 keV). The typical systematic error introduced in the angle A of the cuts in **v** space by the approximation of straight line orbits for the lithium ions is given by the arrows.

CENTRE PANEL: THE SHADED AREAS IN THIS PLOT (WHICH IS IN THE SAME FORMAT AS THE LEFT-HAND PANEL) DENOTE THE AREAS OVER WHICH SAMPLES OF $f^*(\mathbf{v})$ ARE ADVERSELY AFFECTED BY THE LIMITATIONS OF THE DETECTOR RESPONSE.

Measurements of the neutral $f^*(\mathbf{v})$ within the solid and hatched regions require ions moving on cycloidal orbits to be detected at energies which imply arrival angles where the detector efficiency is $\leqslant 10\%$ and $\leqslant 50\%$, respectively. The shaded areas have been mapped to within regions in **v** space where the one-count level becomes large.

RIGHT-HAND PANEL: IN THIS PLOT THE SHADED AREAS OF THE CENTRE PANEL HAVE BEEN SUPERIMPOSED ON THE CONTOURS OF $f^*(\mathbf{v})$ SHOWN IN THE LEFT-HAND PANEL.

can now be used to estimate the total number of neutrals that were released, using equation (18). Assuming for simplicity that $f(\mathbf{v})$ is some constant, f_0, within a sphere in velocity space, of radius v_0, and zero elsewhere, we have

$$N_0 = f_0^* \frac{\tau_p}{G_0} \frac{4}{3} \pi v_0^3 \tag{19}$$

which, taking $f_0^* = 0.2$, $v_0 = 2.5$ km s^{-1} and $\tau_p = 3600$ s gives an estimate $N_0 = 2.99 \times 10^{25}$, in good agreement with expectations (e.g. Krimigis *et al.*, 1982).

We will now consider the effect of the uncertainty in the spacecraft orientation **s**, and of the errors introduced by the straight line orbit approximation, on the above statements. Figure 5 was re-calculated for extreme orientations of **s**, that is, with **s** lying at the limits of the range of possible orientations implied by the uncertainties in the vector components. It was then found that the spread in the typical speeds found for the various cuts in the distribution function varied from the largest of ~ 2.8–1.9 km s^{-1} to the smallest of ~ 2.9–2.3 km s^{-1}. It is interesting, however, to consider the possibility that some orientation of **s** might exist that would distort the contour plot of Fig. 5 into a configuration that no longer appeared to be anisotropic. The most compelling evidence for local

anisotropy found in this analysis is illustrated in Fig. 4, where the upper plot shows large values of the neutral $f(v)$ (at $v_U \sim 2.8$–3.0 km s^{-1}) corresponding to speeds in the lower plot where $f(v)$ is small. We now proceed on the assumption that in the lower plot the neutral $f(v)$ may peak at $V_L \sim 2.0$–2.2 km s^{-1}, but is not observed to do so as the ion detector efficiency is small in this region. We will attempt to calculate the orientation of **s** required to distort neutral velocity space such that the values of $f(v)$ found for these two regions appear at the same speeds. Now from equation (14) it is clear that the location of any given point in neutral velocity space **v** is specified completely by the time t and energy $\varepsilon = EP$ of its corresponding ion measurement, and the location of **s**. Requiring the difference in speeds of any two such points $\mathbf{v}_1$ and $\mathbf{v}_2$ to be zero gives from (14)

$$\hat{\mathbf{s}} \cdot \hat{\mathbf{E}} = \frac{t_2^2(s^2 + P_1^2) - t_1^2(s^2 + P_2^2)}{2s(P_1 t_2^2 - P_2 t_1^2)} \qquad (20)$$

where subscripts 1 and 2 just refer to the two original points in **v** space, and s, the magnitude of the spacecraft separation vector, remains constant as **s** is rotated. Putting values appropriate to $\mathbf{v}_U$ and $\mathbf{v}_L$ given above however yields $|\hat{\mathbf{S}} \cdot \hat{\mathbf{E}}| > 1$, even when errors in s and P are taken into account (compared with these, the error in t is negligible). We therefore conclude that there will always be some local anisotropy in the neutral $f(\mathbf{v})$ derived from the *UKS* ion data whatever value of **s** is chosen.

A further contribution to errors in the derived neutral $f(v)$ is due to the deviation of ion trajectories from the straight line orbit approximation used here. Equation (16) gives the angular displacement γ between the electric field vector passing through the *UKS* position and the line on which the exact ion creation point lies (see Fig. 3). For ions created at some distance from the *UKS* (for which γ is significant), the corresponding displacement in angle A is just the projection of γ into the $\hat{\mathbf{E}}$, **s** plane; this is given on the left hand panel of Fig. 5 for some of the fixed radial cuts in **v** space. This angular displacement is, of course, always in the same sense for all velocity vectors, for a given **E** and **s**. From the figure it is then clear that this error does not significantly affect the interpretation that has been made of the contour plot. The remaining component of the angular displacement γ which is perpendicular to the **E**, **s** plane then would specify more exactly the surface cutting the three-dimensional neutral distribution function over which this measurement is made, and to which the **E**, **s** plane is an approximation.

For completeness, we will briefly compare these results with the more preliminary analysis given by Coates *et al.* (1986). In that analysis (e.g. their Fig. 2), the detected lithium ion energy is shown to increase linearly with time, requiring a shell-like neutral cloud with a constant expansion velocity $v_{ex} \sim 3$ km s^{-1}. For this linear fit to be appropriate, however, data is only used after 9:56:40 U.T., equivalent to spin 4 here, so that the neutrals acting as a source for the detected ions have presumably reached a distance $v_{ex}t \gg |\mathbf{s}|$. The line in velocity space corresponding to measurements made during spin 4 has been marked on the right-hand plot of Fig. 5. The data used in the preliminary analysis hence correspond to measurements in velocity space to the right of this line, which if taken alone does not suggest a significant anisotropy. Now since measurements of the number of counts of lithium ions seen at higher energies will be strongly weighted w.r.t. those at lower energies [from equation (13)], an analysis based simply on the number of counts, as in Coates *et al.*, leads to a larger value for the typical speed of the neutral population lying to the right of the spin 4 line. Finally, from our discussion of the effect of the detector response on the neutral $f(\mathbf{v})$ we can see how the preliminary analysis would indicate that the neutral $f(\mathbf{v})$ was shell-like.

5. SUMMARY

We have so far shown that, for the quiet conditions following the second lithium release, the *UKS* ion data can be used to deduce the neutral velocity distribution function over a restricted region in velocity space. These restrictions are such that it is not possible to determine from this data whether or not the neutral $f(\mathbf{v})$ is shell-like, but it is possible to show that it has a significant local anisotropy. For the most probable orientation of the spacecraft separation vector **s**, typical neutral speeds then vary with direction from ~ 2.8 to 2.1 km s^{-1} as shown in Fig. 5, which, for extreme orientations of **s**, becomes a range of ~ 2.8–1.9 km s^{-1} giving an estimate of the maximum spread in typical speeds, to a range of ~ 2.9–2.3 km s^{-1} giving an estimate of the minimum spread. For the same release, ion measurements from the *IRM* have been used to estimate expansion speeds for the neutral cloud (Paschmann *et al.*, 1986). Being at the release centre, the *IRM* to a good approximation detects ions produced from neutrals which all travel along the same single radial path, that is, along the $-\mathbf{E}$ direction. The *IRM* measurement would then appear as a peak in $f(\mathbf{v})$ which would lie on the $-\mathbf{E}$ axis in Fig. 5, so that the expansion speed of 3.8 km s^{-1} which they derive is therefore not inconsistent with the general anisotropic shape of the contours of $f(\mathbf{v})$ found here

from the *UKS* data. Furthermore, for the first release, which took place during much more disturbed ambient conditions, analysis of the low flux of high energy (5–20 keV) lithium test ions as reported by Möbius *et al.* (1986) has shown that the neutrals acting at a source of these ions moved with a range of expansion speeds of $\sim$2.25–0.65 km s^{-1}, consistent with a neutral cloud that is anisotropic, or that is not shell-like.

Finally, two factors may contribute to the observed anisotropy of the neutral cloud. First, the neutrals are expelled from a nozzle at one end of the canisters containing the initial release chemicals. The ejection time of $\sim \frac{1}{5}$ s is sufficiently short that any slow tumbling motion of the canisters probably does not scatter the beam of neutrals emitted from the nozzle. On the other hand, the $\sim$ 10 min time delay between canister ejections from the *IRM* and ignition implies that the canisters could be at any arbitrary orientation as the neutrals are released. Second, although the mass of released lithium vapour is negligibly small compared with the canister mass, the mass of other constituents in the release compound which is ignited is not, so that emission of the latter would cause the canister to recoil, reducing the speeds of the escaping lithium vapour.

Acknowledgements—The authors are most grateful to M. W. Dunlop, M. Six, W. A. C. Mier-Jedrzejowicz and R. P. Rijnbeek for their contribution to the analysis of the magnetometer data, and to S. W. H. Cowley for valuable discussions of this work.

REFERENCES

Bryant, D. A., Krimigis, S. M. and Haerendel, G. (1985) Outline of the *Active Magnetospheric Particle Tracer Explorers* (*AMPTE*) Mission. *IEEE Trans. Geosci. Remote Sensing* **GE-23**, 177.

Coates, A. J., Bowles, J. A., Gowen, R. A., Hancock, B. K., Johnstone, A. D. and Kellock, S. J. (1985) *AMPTE–UKS* three dimensional ion experiment. *IEEE Trans. Geosci. Remote Sensing* **GE-23**, 287.

Coates, A. J., Johnstone, A. D., Smith, M. F. and Rogers, D. J. (1986) *AMPTE–UKS* ion experiment observations of lithium releases in the solar wind. *J. geophys. Res.* **91**, 1331.

Haerendel, G., Valensuela, A., Bauer, O. H., Ertl, M., Föppl, M., Kaiser, K.-H., Lieb, W., Loidl, J., Melzner, F., Merz, B., Neuss, N., Parigger, P., Rieger, E., Schöning, R., Stöcker, J., Wiezorrek, E. and Molina, E. (1985) The Li/Ba release experiments of the ion release module. *IEEE Trans. Geosci. Remote Sensing* **GE-23**, 253.

Krimigis, S. M., Maerendel, G., McEntire, R. W., Paschmann, G. and Bryant, D. A. (1982) The *Active Magnetospheric Particle Tracer Explorers* (*AMPTE*) program. *EOS Trans. A.G.U.* **63**, 843.

Lühr, H., Southwood, D. J., Klöcker, N., Acúna, M., Häusler, B., Dunlop, M. W., Mier-Jedrzejowicz, W. A. C., Rijnbeek, R. P. and Six, M. (1986) *In situ* magnetic field measurements during *AMPTE* solar wind Li^+ release. *J. geophys. Res.* **91**, 1261.

Möbius, E., Hovestadt, D., Klecker, B., Scholer, M., Glocker, G., Ipavich, F. M. and Lühr, H. (1986) Observation of lithium pick-up ions in the 5 to 20 keV energy range following the *AMPTE* solar wind releases. *J. geophys. Res.* **91**, 1325.

Paschmann, G., Carlson, C. W., Baumjohann, W., Curtis, D. W., Sckopke, N. and Haerendel, G. (1986) Plasma observations on *AMPTE/IRM* for the lithium releases in the solar wind. *J. geophys. Res.* **91**, 1271.

Southwood, D. J., Mier-Jedrzejowicz, W. A. C. and Russel, C. T. (1985) The fluxgate magnetometer for the *AMPTE* U.K. subsatellite. *IEEE Trans. Geosci. Remote Sensing* **GE-23**, 301.

APPENDIX A

Here we briefly itemize those uncertainties in the parameters used in equation (13), which are considered to be negligibly small for the purposes of the analysis given in this paper.

(1) The releases are made from two canisters separated by $\sim$ 2 km (cf. *UKS–IRM* separation of $\sim$ 30 km) such that the lithium neutrals start from a small region of space to a reasonable approximation.
(2) The release produces a collisionless, instantaneous neutral cloud (see Section 2).
(3) The release time is known from the magnetometer data to within 1 s, giving only a $\sim$ 2% error in the neutral **v**.
(4) The time variation of the $\hat{\mathbf{E}}$ direction over the entire period during which Li ions are observed is only $\sim 6°$ on average.
(5) The time variation of $|\mathbf{E}|$ over the few second flight times of the ions is in all cases small, $\sim$ 2%.
(6) Changes in **E** over timescales shorter than the 10 s resolution of the solar wind velocity measurements are assumed to be of order the $< 10\%$ changes in **B** (sampled 16 times per second).
(7) Spatial variations of **E** due to localized flow perturbations are always on a larger scale than the ion flight paths.
(8) Uncertainty in the measured **E** is smaller in direction than (4) and in magnitude produces a smaller error in path lengths P_i than the bin widths $dP_i = d\varepsilon_i/E$ themselves.

APPENDIX B

Here, we use the equations describing cycloidal orbits (1) and (2) to obtain a relationship between the GSE azimuthal angle with which an incoming ion arrives at the detector, and its energy. It is convenient to work in terms of the angle δ between the ions' velocity vector **v** and the ambient electric field, where $\sin\delta = v_{\beta}/|\mathbf{v}|$, which can be expressed in terms of the ion energy $\varepsilon = \varepsilon(t)$, since

$$\frac{|\mathbf{v}|}{v_{\perp}}\sin\delta = \sin\delta\left(\frac{m_p}{m_{Li}}\frac{\varepsilon}{\varepsilon_{sw}}\frac{1}{\sin^2\psi}\right)^{1/2} = 1-\cos\Omega t \quad \text{(B1)}$$

and

$$\varepsilon = \frac{1}{2}\frac{m_{Li}}{q}|\mathbf{v}|^2 = \frac{1}{2}\frac{m_{Li}}{q}(v_\alpha^2 + v_\beta^2)$$

$$= \frac{2m_{Li}}{m_p}\varepsilon_{sw}\sin^2\psi(1-\cos\Omega t) \tag{B2}$$

where ψ is the angle between $\mathbf{B}$ and $\mathbf{v}_{sw}$, and $\varepsilon_{sw} = m_p\mathbf{v}_{sw}^2/2q$, the ambient solar wind convection energy. We then have

$$\varepsilon = \frac{4m_{Li}}{m_p}\varepsilon_{sw}\sin^2\psi\sin^2\delta. \tag{B3}$$

We can now project the ion cycloidal velocity vector $\mathbf{v}$ into the GSE equatorial (x, y) plane. Since the velocity vector $\mathbf{v}$ lies in the α, β plane, we have

$$\mathbf{v} = v_\alpha\hat{\boldsymbol{\alpha}} + v_\beta\hat{\boldsymbol{\beta}} = v_\alpha\frac{\mathbf{E}}{|\mathbf{E}|} + v_\beta\frac{\mathbf{E}\wedge\mathbf{B}}{|\mathbf{E}\wedge\mathbf{B}|} \tag{B4}$$

which, in terms of GSE (x, y, z) components, becomes

$$\mathbf{v} = \hat{\mathbf{x}}\left(v_\alpha\frac{E_x}{E} + v_\beta\frac{v_{\perp_x}}{v_\perp}\right) + \hat{\mathbf{y}}\left(v_\alpha\frac{E_y}{E} + v_\beta\frac{v_{\perp_y}}{v_\perp}\right) + \hat{\mathbf{z}}\left(v_\alpha\frac{E_z}{E} + v_\beta\frac{v_{\perp_z}}{v_\perp}\right) \tag{B5}$$

where x, y and z subscripts all refer to the GSE coordinate system. The GSE x component of $\mathbf{v}$ is just

$$v_{\perp_x} = v_{sw}\left(\frac{v_{swx}}{v_{sw}} - \cos\psi\frac{B_x}{B}\right) \tag{B6}$$

and similarly for the y and z components so that the azimuthal angle of $\mathbf{v}$ measured in the GSE equatorial plane, ϕ, is given by

$$\tan\phi = \frac{v_y}{v_x} = \frac{\dfrac{E_y}{E} + \tan\delta\dfrac{v_{\perp_y}}{v_\perp}}{\dfrac{E_x}{E} + \tan\delta\dfrac{v_{\perp_x}}{v_\perp}} \tag{B7}$$

and the polar angle θ of $\mathbf{v}$ measured from the z GSE axis is given by

$$\tan\theta = \frac{(v_x^2 + v_y^2)^{1/2}}{v_z} = \frac{\left[\left(\dfrac{E_x}{E} + \tan\delta\dfrac{v_{\perp_x}}{v_\perp}\right)^2 + \left(\dfrac{\mathbf{E}_y}{E} + \tan\delta\dfrac{v_{\perp_y}}{v_\perp}\right)^2\right]^{1/2}}{\left(\dfrac{\mathbf{E}_z}{E} + \tan\delta\dfrac{v_{\perp_z}}{v_\perp}\right)}. \tag{B8}$$

Equations (B7) and (B8) then specify the GSE azimuthal and polar angles of incoming ions on cycloidal orbits as a function of their energy, and of the ambient electromagnetic fields through equation (B3).